A Study on the Development of Measurement Techniques for Thermal Flows in MEMS

Han-Seo Ko*, Sang-Sik Yang, Jai-Suk Yoo*** and Hyun-Jung Kim†**

Abstract - A review on advanced flow visualization techniques is presented particularly for applications to micro scale heat and mass transport measurements. Challenges, development and applications of micro scale visualization techniques are discussed for the study of heating/evaporating thin films, a heated micro channel, and a thermopneumatic micro pump. The developed methods are (1) Molecular Tagging Fluorescence Velocimetry (MTFV) using 10-nm caged seeding molecules (2) Micro Particle Velocimetry (MPIV) and (3) Ratiometric Laser Induced Fluorescence (LIF) for micro-resolution thermometry. These three methods are totally non-intrusive techniques and would be useful to investigate the temperature and flow characteristics in MEMS. Each of these techniques is discussed in three-fold: (1) its operating principle and operation, (2) its application and measurement results, and (3) its future challenges.

Keywords: Fluorescence, Laser, LIF, MEMS, Micro Fluidics, Micro PIV

1. Introduction

Among the heat transport devices presently under consideration for future critical use in dissipating high intensity heat energy, massive cooling electronics for unmanned flight vehicles or hypersonic re-entry vehicles under extreme thermal stresses, what is most expected is to utilize the latent heat of vaporization via liquid-vapor phase change [1]. For a variety of these devices, the phase change occurs commonly through microscale thin film evaporation on a liquid-saturated porous or mesh media where capillary forces provide the driving potential for the liquid flow from the condenser to the evaporator.

Thus, heated and evaporating thin film conforms to the basic model for two-phase heat/mass transfer in heat pipes and various Capillary-Pumped Heat Transport Devices (CPHTD) that involves micro fluidic and micro scale heat transfer. The capillary region is characterized by normal stresses dominated by surface tension whereas the adsorbed film region is characterized by normal stresses dominated by intermolecular forces. The dynamics of the capillary region have been extensively studied and modeled. The adsorbed film region may be characterized by adsorption isotherms and is typically a static molecular film that has no significant impact on the thermo-fluid dynamics. Of these three regions, the transition film region of up to an order of 1-μm thick is the least understood, yet the most crucial in that the majority of heat and mass transport is known to take place in this micro-region.

In addition, the desired or predicted cooling capacity is rarely achieved and the device is subjected to premature "dry-out" resulting from the excessive thin film instability and degraded wetting ability [2]. The speculation here is that the dynamics associated with fluid motion (phoresis) in the vicinity of the evaporating meniscus can detrimentally affect the driving capillary potential by degrading the wetting ability of the working fluid [3, 4]. The non-isothermal liquid-vapor interfacial temperatures, quite possibly occurring near the contact line, yield surface tension gradients along the interface, with increasing slope toward a cooler region away from the thin film region. For example, if the pore wall is heated, the relatively cooler pore center region, with higher surface tension, can act to pull down the hotter and evaporating thin film region with lower surface tension. Therefore, these surface tension gradients result in thermocapillary phoresis, or the pulling down action to the thin film, which can degrade the wetting ability of the liquid [5-8].

In order to understand and resolve the thin film instability/dry-out problems, which has been the major obstacle to a more practical use of two-phase heat transfer for the aforementioned critical uses, microscale measurements will be necessary for the coupled effects of thermal transport, Marangoni stress, and viscous stress on the shape and fluid flow of an evaporating meniscus from the transition film

† Corresponding Author: Division of Mechanical Engineering, Ajou University, Woncheon-dong, Yeongtong-gu, Suwon 443-749, Korea. (hyunkim}@ajou.ac.kr)
* School of Mechanical Engineering, Sungkyunkwan University, 300 ChunChun-Dong, JangAn-Gu, Suwon, 440-746, Korea. (hanseoko@yurim.skku.ac.kr)
** Division of Electronics Engineering, Ajou University, Woncheon-dong, Yeongtong-gu, Suwon 443-749, Korea. (ssyang@ajou.ac.kr)
*** Division of Mechanical Engineering, Ajou University, Woncheon-dong, Yeongtong-gu, Suwon 443-749, Korea. (jyoo@ajou.ac.kr)
Received: September 29, 2005 ; Accepted: March 7, 2006

region through the meniscus region to a sufficient degree that the data may be used to benchmark the validation of theoretical models for local evaporative flux and inner scale thermo-fluid dynamics of an evaporating contact line. To that end, another objective is to develop a unique microscale flow field measurement technique with which to collect the fluid flow data in the expanded transition film region. Therefore, advanced microscale optical techniques must be considered to measure the film thickness, heat transport, and liquid velocity fields in the transition film region of an extended meniscus.

In this paper, related optical diagnostic techniques will be presented to guide researchers in the measurement of micro-scale velocity and temperature. Each visualization technique will be discussed for its principle, system development, measurement results, and future challenges for more advanced studies.

2. Molecular Tagging Fluorescence Velocimetry(Mtfv)

Fig. 1-a illustrates a schematic of the basic experimental setup for MTFV [9, 10], which intrinsically resembles the fluorescence microscopy that was developed in the early part of the 20th century, except that a monochromatic laser has substituted the band pass-filtered light source.

A triple harmonic ultraviolet Nd:YAG laser pulse of 8-mm diameter (λ = 355 and adjustable from 100 μJ up to 10 mJ) illuminates the test field with a pulse duration of 5 to 6 nanoseconds. A density filter reduces the beam power to avoid damage to the optical elements and an aperture reduces the beam diameter down to 5 mm to eliminate noise and diffused light from the edge of the beam. An ultraviolet convex lens with a focal length of 100 mm focuses the 5-mm diameter laser beam to a 20-μm diameter

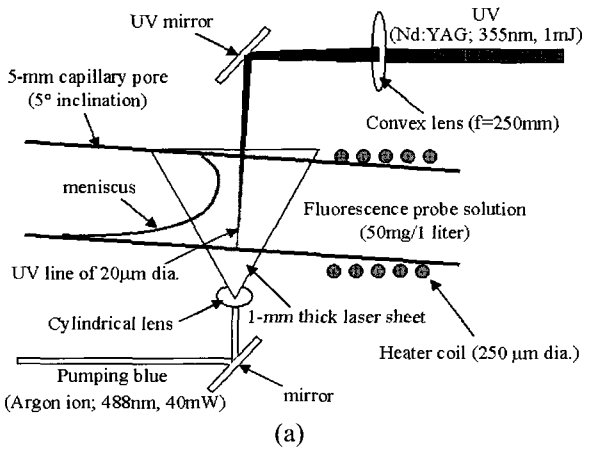

(a)

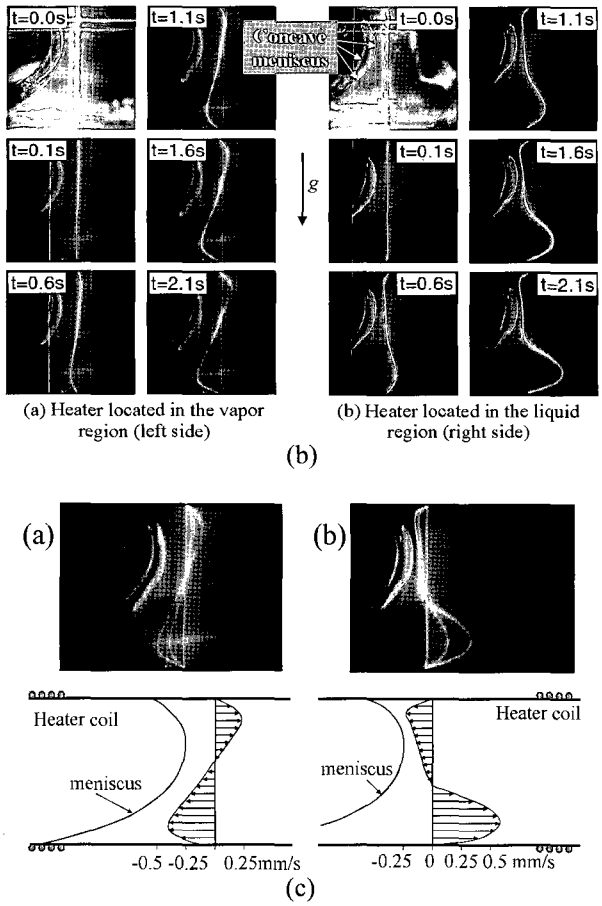

Fig. 1 Schematic illustration of Molecular Tagging Fluorescence Velocimetry (a), Lagrangian mapping of the thermally induced flow evolution (b), and digitally determined velocity profiles (c).

at the test section. The test section is a capillary pore mounted on a three-degrees-of-freedom positioning system that is also 360° rotational. A 1-mm diameter CW argon-ion blue laser beam (λ= 488 nm at 40 mW) illuminates the capillary pore test section from the opposite side of the ultraviolet laser. The blue beam is additionally filtered by a narrow band-pass interference filter to remove extraneous wavelengths of light incidentally produced by the Argon-ion laser that can induce uncaging of the caged fluorescent dye. A cylindrical lens creates a thin blue laser sheet to illuminate uncaged fluorescence dyes in the test section. The UV beam and thin blue sheet vertically pass through the symmetric center plane of the capillary pore.

The fluorescent dye used for the experiment was a Dextran, DMNB-caged anionic fluorescein molecular dye with a molecular weight of 10,000 grams/mole and manufactured by Molecular Probe, Inc. The absorption (pumping) maximum of the dye occurs at 494 nm, and the emission (fluorescence) maximum occurs at 518 nm. The probe is water-soluble and is mixed to a concentration of 50 mg per liter of distilled, deionized water. This concentration is sufficient to induce images that are bright enough to be

easily seen by the naked eye and captured by the CCD camera in a totally dark environment. Note that the optimum probe concentration depends on many local laboratory conditions including the pumping light intensity, test section dimensions, optical window characteristics, flow convection and diffusion, and sensitivity of recording means.

The fluorescence rise time for the uncaging evolution was estimated to be as short as 1 ms, i.e., the fluorescence intensity quickly reaches a substantial level of the saturated intensity after the probe is short-pulsed by UV. The evolution thereafter is a rather slow process that takes up to 0.5 sec until all the probes are fully uncaged or saturated [11]. The degree of uncaging achieved during the first quick rise within 1 ms or so is sufficient to produce conceivable fluorescence images. Therefore, the temporal uncertainty due to the rise time on the order of 1 ms should be limited to an order of 0.1% of the true velocity tracking. The emission delay of the fluorescence after pumping is negligible in the nanosecond range and the spontaneous radiative lifetime of fluorescence in water is approximately 5 ns [12]. The caging compound is inherently unstable and its instability is increased with exposure to high temperatures and ultraviolet light sources, including ambient light. The probe should be handled in a dark environment and stored at temperatures around –20°C in the original powder and at around –4°C in the water solution state to minimize spontaneous uncaging. The heating of the test fluid to induce the thermal flow may cause a degree of uncaging of the probe, which creates vaguely fluorescent background images. The actual fluorescence images of the UV-uncaged probe are substantially brighter than the illusive background, which has been digitally subtracted from the recorded images. The fluorescence images in Fig. 1-b show sequential images of thermal bulk flows recorded at the vertical center plane of the capillary pore. The first frames are taken at t = 0 when the UV pulse is applied for uncaging and the initial thin line of the uncaged dye molecules is shown with the intense reflection of the UV from the pore inside the glass surface. The subsequent frames represent the evolution of the uncaged dye as dictated by convection and diffusion. An interesting observation is that the lower part of the bulk flow is moving toward the heater location on the symmetry plane while the upper bulk flow is moving away from the heater for both cases of heater locations. Fig. 1-c presents velocity vector fields determined by digital processing of the sequential images.

3. Micro PIV

In the presented study, the micro PIV system was developed to investigate flow features in a micropump. While the concept of Micro PIV is basically similar with the regular PIV, scaling down the PIV brings forth several problems. The development of micro PIV is well-described in Ref. [13]. Fig. 2 indicates the visualized image of a micropump inside that was taken from the bottom. The measured areas are denoted by a red line box for the outlet and inlet region. Fig. 3 shows the schematic of a μ-PIV system that was utilized in the present study. 10-μm fluorescence particles that have an excitation peak at 525-nm and an emission peak at 565-nm were seeded in the working fluid of the micro pump. These absorption and emission bandwidths partially overlap with each other. To detect fluorescence signals exclusively, the fluorescence detection band must be separated from the emission and absorption bandwidths, to the maximum extent possible.

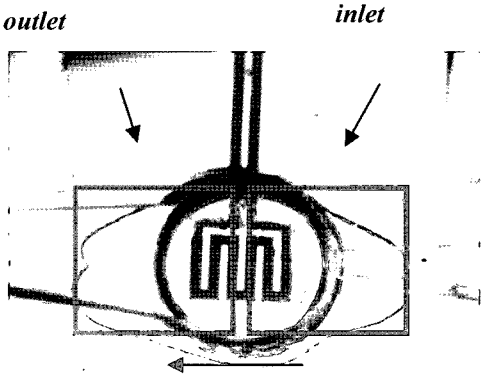

Fig. 2 The visualized image of a u-pump inside

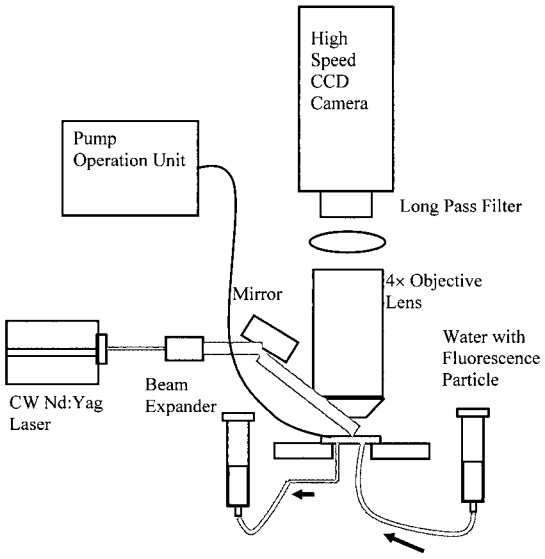

Fig. 3 The schematic of an μ -PIV experimental apparatus

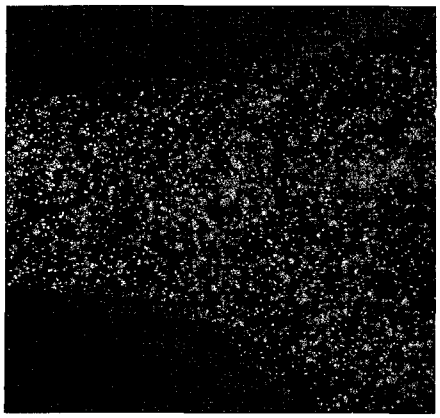

Fig. 4 The visualized image of particles

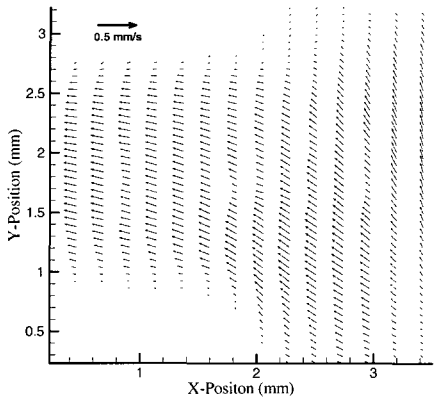

(a) Outlet

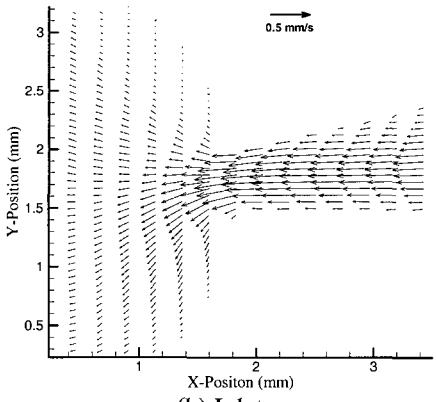

(b) Inlet

Fig. 5 The measured average velocity field for **1 Hz** pumping frequency with 50% duty ratio

The selection was made for the long pass filter that transmits wavelengths longer than 532-nm. This filtering process passes a pure fluorescence image of seeding particles without accepting scattering of the background illumination of the excitation light. In addition, using visible light with a wavelength of 532-nm to illuminate the particles means that the light scattering is in the Rayleigh range. The Rayleigh scattering intensity decreases with d^6 as the diameter of the seeding particles decreases while the fluorescence signal is much stronger than the Rayleigh scattering for sub-micron seeding particles. Therefore, using fluorescence seeding particles is almost essential to obtain high image intensity for micro PIV as shown in Fig. 4 The high speed 512 × 480 CCD camera with a 4× magnification microscope objective lens was used for recording particle images. A 22-μm thin depths of field microscope objective lens decided the 2-D measure plane instead of using a laser sheet [15]. Due to the pumping by diaphragm movement, periodic unsteady flows are expected within the pump chamber. For that reason, a CW Nd:Yag laser with wavelength 532 nm was adopted. The particle images were recorded at 60 fps. During the pump operation and measurement, inlet and outlet reservoirs were maintained at identical height in order to obtain the zero pressure within the micropump.

Fig. 5 shows the 360 images averaged velocity field for 1Hz pumping frequency with 50% duty ratio for inlet and outlet regions. This averaged velocity shows the net flow direction from the alternative forward and backward flow during the operation period. The left hand side direction of velocity in Fig. 5 indicates that the sum of the forward direction flow is larger than that of the backward flow during the operation time.

The maximum velocity at a diffuser channel is 57-μm/s. Due to the small entrance size the maximum velocity of the nozzle channel is about three times larger than one of the diffuser channels, satisfying the continuity. From these Fig.s, some spurious vectors are seen in the chamber region. As we described in 2 and 3, the chamber and channel height is 500 μm and 30 μm, respectively and the measured 2-dimensional plane was the middle position in channels, which was approximately 470 μm away from the diaphragm. Therefore, although the flow was expected to be made nearly along the channel length direction in the measured plane, it is considered that the 3-dimensional flow effect existed in that plane due to the 3-dimensional direction diaphragm vibration.

To investigate the transient flow pattern by the vibrating diaphragm, the x direction velocity of the center point of the channel is plotted with respect to time in Fig. 6 As shown in Fig. 6, the oscillating flow pattern can be identified. From Fig. 6, negative values indicate the forward direction of the flow from the chamber. Conversely, the backward direction of the flow is denoted by the positive value. Although water is rejected by diaphragm deflection from the outlet, there then exists backward flow which returns to the chamber through the outlet when the diaphragm is restored. This backward flow from the outlet appears smaller than the rejected

flow (forward direction flow) from the outlet in each pumping period. This fact results from the flow resistance difference between the nozzle/diffuser elements [15 - 16]. In other words, the unfavorable pressure gradient exists in the backward flow direction for the outlet and thereby retards the

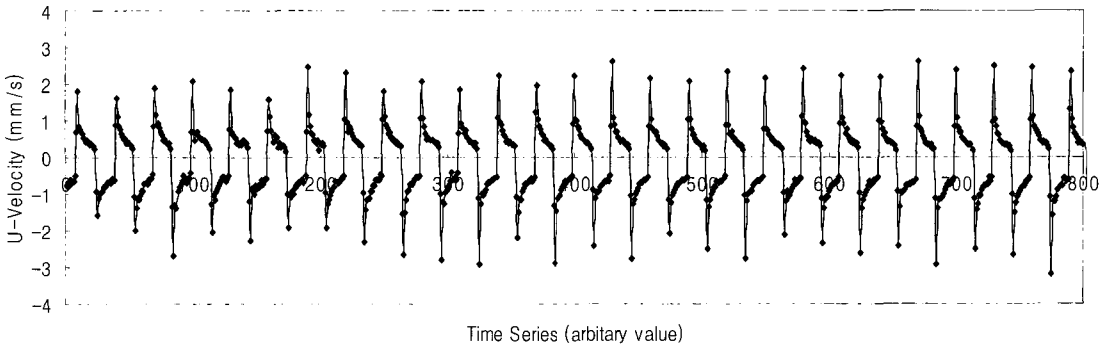

Fig. 6 The instantaneous x direction velocity time series (Frequency: 1.0 Hz, Duty: 50%)

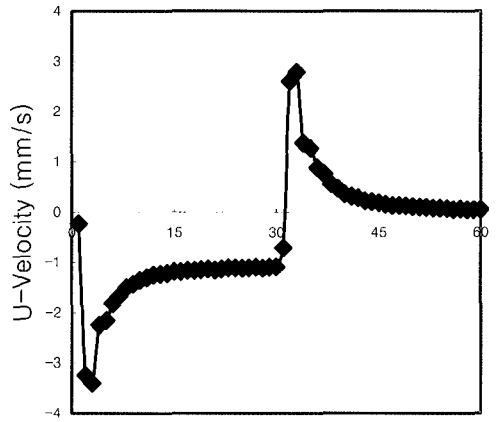

(a) Outlet

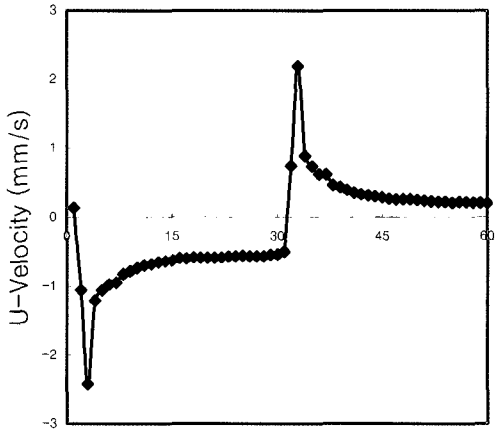

(b) Inlet

Fig. 7 The phase averaged velocity field (Frequency: 1.0 Hz, Duty: 50%)

backward flow. Conversely, the forward direction flow can be accelerated by the favorable pressure gradient. This is vice versa in the inlet channel. The pumping period in Fig. 6 is worth while to be phase-averaged. The smooth curve that represents the averaged flow pattern of the micropump during the measurement time is obtained through the phase average process as shown in Fig. 7 One can identify more clearly that the area of negative value is larger that one of positive value. But this sum of the area indicating the net flow rate is small. In principle, the unfavorable pressure gradient results from the inertia effect of the flow [17]. Due to the small scale of the micropump, the Reynolds number of this flow is very low. Therefore, the amount of unfavorable pressure is small in the micropump. The flow resistance difference between the nozzle and diffuser is considered to be increased for the enhancement of pump efficiency. It is expected that the angle of the nozzle inlet and outlet diffuser must be wider to increase this sum of the curve area in Fig. 7 [18 - 19]. Therefore, if the structure of the micropump is modified to have a diffuser and nozzle with a wider angle, the flow rate of the type of thermopneumatic micropump is expected to be enhanced.

4. Ratiometric Laser Induced Fluorescence (LIF) Thermometry

The ratiometric LIF, as it has come to be known as originated from the field of biology, is also called dual emission LIF [20] and two-color LIF [21]. The latter article presented a calibration uncertainty of ±1.5 K over a 25 K temperature range. The present LIF system uses Rhodamine-B [absorption peak at 554-nm and emission peak at 575-nm] as a temperature sensitive dye, as high as 2-% emission intensity change per K, and Rhodamine-110 [absorption peak at 496-nm and emission peak at 520-nm] as a temperature insensitive dye, as low as 0.13%/K. Both fluorescent dyes are pumped by the "blue" Ar-ion CW laser light band-peaked at 488-nm.

In the absence of the pH-dependence of both dyes, the intensity ratio of the two fluorescence emissions is given as:

$$\frac{I_{rhb}}{I_{rh110}} = \frac{I_{0rhb}\varepsilon_{rhb}[c]_{rhb}Q_{rhb}}{I_{0rh110}\varepsilon_{rh110}[c]_{rh110}Q_{rh110}} \quad (1)$$

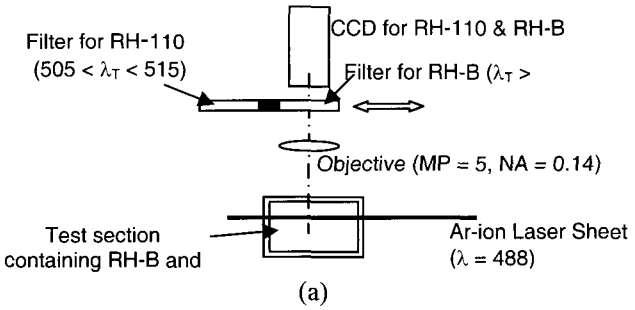

(a)

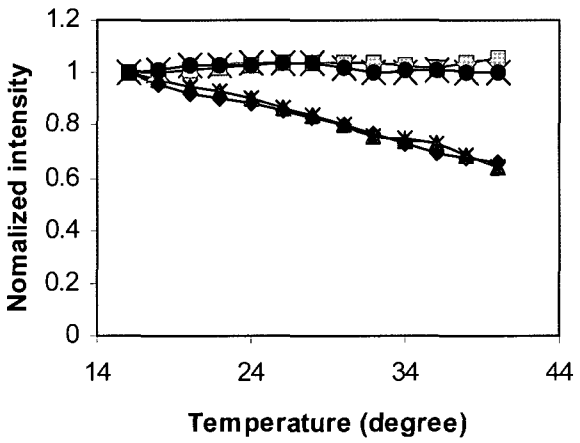

(b)

Fig. 8 Schematic illustration of the ratiometric LIF thermometry system (a), and calibration intensity curves of RH-B and RH-110 dyes versus temperature (b).

where the ratio of the absorption spectral intensity, I_{0rhb}/I_{0rh110}, is invariant when a single illumination source is used for both dyes, and the molar absorptivity ε is nearly independent of temperature [22]. For a fixed concentration ratio of the two dyes, $[c]_{rhb}/[c]_{rh110}$, the fluorescence intensity ratio, I_{rhb}/I_{rh110}, will only depend on the quantum efficiency ratio, Q_{rhb}/Q_{rh110}, which may be correlated to temperature. A careful calibration is needed to determine a functional correlation between the fluorescent intensity ratio (I_{rhb}/I_{rh110}) and temperature of the test medium containing small concentrations of both fluorescent dyes.

Table 1 Dependence of the calibration uncertainties with 95-% confidence level on the interrogating cell size

Interrogation cell (pixels)	Spatial Resolution (μm)	Intensity Ratio Uncertainties	Temperature Uncertainties (°C)
1 by 1	4.7 × 4.2	±0.143	±5.635
10 by 10	47 × 42	±0.056	±2.964
32 by 24	150 × 100	±0.043	±1.967
64 by 48	300 × 200	±0.033	±1.496
128 by 96	600 × 400	±0.022	±1.006
256 by 192	1200 × 800	±0.009	±0.412
320 by 240	1500 × 1000	±0	±0

The single-camera system (Fig. 8-a) sequentially detects each fluorescence signal by alternating the two band-pass filters, a long-pass filter (λ_T > 560 nm) for Rh-B detection and a narrow band-pass filter (505 nm < λ_T < 515nm) for Rh-110 detection [23]. Since the camera detects para-normal incident rays, the spectral dispersion problem is minimized and the need for point-by-point calibration is unnecessary. Also, the single-camera system requires less attention to image coincidence and is relatively insensitive to external vibrations. The primary limitation of the simplified system is resulted from the sequential image recording, and the single-camera system is unable to handle unsteady thermal problems. The single-camera ratiometric LIF system, however, is believed to be more reliable and convenient than the dual camera setup [21] for investigating steady thermal problems.

A calibration experiment is necessary to determine the correlation between the fluorescence intensity ratio and temperature using a constant-temperature cuvette at a specified temperature. An interline transfer monochromatic CCD camera (maximum 640 x 480 pixels resolution, approximately 9.0 μm pixel size, Sony XC-73) with a Mitutoyo 5x objective lens (NA = 0.14) having an extended working distance of approximately 37-mm was used to record images of approximately 3.0-mm × 2.0-mm. Note that due to the chemical and photochemical decomposition, the emission intensity of fluorescence dye degrades during repeated excitation and emission transitions. Therefore, a fresh mixture of fluorescence dyes was used for each test run [24].

Fig. 8-b plots fluorescence intensity for the two dyes (Rh-B and Rh-110) against a temperature range of 16°C to 40°C. Each data point represents the average intensity of the central 1.5-mm x 1.0-mm field-of-view (320 by 240 pixels), in order to exclude the potentially degraded image of the off-axis region, averaged for ten (10) recorded images. The discrepancy between the three calibration data sets is less than 5%. Though the entire calibration test section should remain ideally at a uniform temperature, the aforementioned non-ideal optical and thermal factors may result in slight spatial nonuniformity in the fluorescence intensity. These non-ideal factors include nonuniformity in the background illumination, which cannot be completely abated, inherent fluorescence intensity variations due to the thermal drift of dye molecules caused by small temperature gradients in the cuvette, and by imperfections and unsteady noise in the CCD pixels.

Assuming a normal distribution of the measured temperature data scattered around the expected value (m),

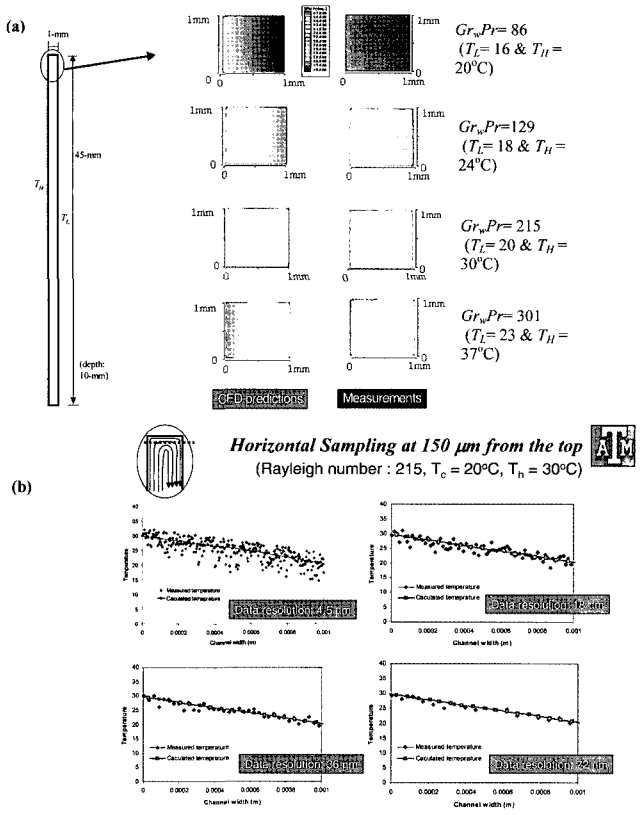

Fig. 9 Calculated (the left column) and measured (the right column) temperature contours for the top 1.0-by 1.0-mm region of a test cuvette with different wall temperatures (a), and measured temperature profiles for different data resolutions for $Gr_w Pr$ = 215; T_L = 20°C and T_H = 30°C (b)

Table 2 Root-mean-square (r.m.s.) fluctuations of the measured temperature data from the predicted values for different spatial resolutions [$Gr_w Pr$ = 215; T_L = 20 °C and T_H = 30°C].

Spatial resolution (h x v; μm x μm)	0.15-mm below the top	0.85-mm below the top
19 x 19	2.377 °C	2.306 °C
38 x 38	1.574 °C	1.566 °C
76 x 76	0.999 °C	0.924 °C

the calibration uncertainty levels are estimated based on a 95%-confidence level standard deviation ($\pm 2\sigma$). Table 1 presents the calibration uncertainties depending on the interrogation cell sizes, with the maximum uncertainty shown for the pixel-by-pixel variation (4.7-μm by 4.2-μm spatial resolution) and zero uncertainty when averaged for the whole calibration field-of-view (1.5-mm by 1.0-mm spatial resolution). Each uncertainty value represents the average across the tested temperature range from 16 to 40 $^\circ C$, and ten images at each temperature. The spatial uncertainties exhibit an adverse dependence on the interrogating cell size, showing dramatic decrease with increasing interrogation cell size. For example, the calibration uncertainty decreases from ± 1.967 °C for 150-μm by 100-μm interrogation cell to ± 0.412 °C for 1200-μm by 800-μm interrogation cell.

The test cuvette (Fig. 9-a) has dimensions of 1-mm wide (w), 10-mm deep (d), and 45-mm high (h). Each of the two sidewalls (10-mm deep and 45-mm high) is maintained at a different temperature by conduction from an attached copper jacket through which water circulates to and from a controlled thermobath. The top and bottom surfaces of the cuvette are insulated to provide an adiabatic condition. The temperature differential between the two sidewalls establishes a steady, thermally-driven buoyant flow. The experimental results are compared with numerical predictions (FLUENT) to locally and quantitatively examine the measurement accuracy and spatial resolution. Fig. 9-a indicates a comparison between the calculated (the left column) and the measured (the right column) temperature distributions for the top 1.0-mm by 1.0-mm square region of the test cuvette. Four diverse wall temperature differentials, 16-20°C, 18-24°C, 20-30°C and 23-37°C, are considered with their corresponding Grashof-Prandtl number, $Gr_w Pr \equiv \frac{g\beta\Delta T w^3}{\nu^2} \cdot \frac{\nu}{\alpha}$ = 86, 129, 215, and 301, respectively (at 300K, the expansion coefficient, β = 2.76 · 10^{-4} K^{-1}, the kinematic viscosity of water, ν = 8.567 · 10^{-7} m^2/s, the thermal diffusivity, α = 1.470 · 10^{-7} m^2/s, and the channel width, w = 1.0 mm). The measured and calculated temperature contours indicate fairly good agreement with each other in that the temperature contours gradually deviate from the vertically stratified distributions with increasing $Gr_w Pr$.

Fig. 9-b shows local and more quantitative comparisons between the measured and calculated temperature profiles at 0.15-mm (the left column), and 0.85-mm (the right column) below the top, for a representative case of $Gr_w Pr$ = 215. To examine the measurement uncertainties as a function of the spatial measurement resolution, the original pixel-by-pixel data are combined to 4x4, 8x8, and 16x16 -pixeled interrogation cells, corresponding to the spatial resolution of 19-μm (H) by 19-μm (V), 38-μm by 38-μm, and 76-μm by 76-μm, respectively. Note that the spatial resolution for numerical calculations is remained as 58.8-μm (H) by 83.3-μm (V) for all of the cases. The data fluctuations should decrease with increasing number of the spatial samplings and the uncertainties are proportional to $1/\sqrt{N}$, for the case of multiple (N) samplings with N

approaching to infinity. The root-mean-square (r.m.s.) fluctuations of the measured temperature data, from the calculated predictions, demonstrate persistent reduction from over 2°C to below 1°C, with increasing spatial resolution from 19-μm square to 76-μm square (Table 2).

5. Future Challenges

Itemized future challenges are presented for the above-discussed six different microscale visualization techniques:

1. Molecular Tagging Fluorescence Velocimetry (MTFV): Reduction of the UV beam diameter to 1-μm order for improved lateral as well as depthwise measurement resolutions.
2. Micro PIV: Resolve the optical window for visualization and resolve "out of focus" effect for correlating seeding particles.
3. Ratiometric Laser Induced Fluorescence (LIF) Thermometry: Resolve the inconsistency of the pumping light illumination between the calibration and the experimental conditions.

These challenges may not be resolved in a straightforward approach as they are literally quite "challenging," but certainly they are worthwhile attempting to improve either by the author or readers of this article.

Acknowledgment

This material is based on the work supported by a grant of the Korea Science and Engineering Foundation (R05-2004-000-11406) and the National Research Laboratory (Thermo-mechanical Properties Measurement Laboratory), established by the Korea Institute of Science and Technology Evaluation and Planning.

References

[1] Personal communications, Dr. D. M. Pratt, Wright-Patterson AFB, Ohio, 2002.

[2] D. M. Pratt, W. S. Chang, and K. P. Hallinan, "Effects of Thermocapillary Stresses on the Capillary Limit of Capillary-Driven Heat Transfer Devices," *Proc. 11th Int. Heat Tran. Conf.* (Kyongju), pp. 201-211, August 1998.

[3] H. B. Ma, D. M. Pratt, and G. P. Peterson, "Disjoining Pressure Effect on the Wetting Characteristics in a Capillary Pore," *Microscale Thermophysics Engineering*, vol. 2, no. 4, pp. 283-297, 1998.

[4] D. M. Pratt, and K. P. Hallinan, "Thermocapillary Effects on the Wetting Characteristics of a Heated Curved Meniscus," *Journal of Thermophysics and Heat Transfer*, vol. 11, no. 4, pp. 519-525, 1997.

[5] P. Ehrhard and S. H. Davis, "Non-Isothermal Spreading of Liquid Drops on Horizontal Plates," *Journal of Fluid Mechanics*, vol. 229, pp. 365-388, 1991.

[6] L. M. Hocking, "On Contact Angles in Evaporating Liquids," *Physics of Fluids*, vol. 7, no. 12, pp. 2950-2955, 1995.

[7] A. K. Sen, and S. H. Davis, "Steady Thermocapillary Flows in Two-Dimensional Slots," *Journal of Fluid Mechanics*, vol. 121, pp. 163-186, 1982.

[8] D. M. Anderson, and S. H. Davis, "Local Fluid and Heat Flow Near Contact Lines," *Journal of Fluid Mechanics*, vol. 268, pp. 231-265, 1994.

[9] J. S. Park, C. McCarty, K. D. Kihm, and D. M. Pratt, "Lagrangian Flow Mapping of Heated Capillary Pore and Thin Film Using Molecular Fluorescence Velocimetry (MFV)," *Journal of Heat Transfer*, vol. 122, pp. 421-423, 2000.

[10] J. S. Park, K. D. Kihm, and D. M. Pratt, "Molecular Tagging Fluorescence Velocimetry (MTFV) Technique to Measure Micro-Scale Thermal Flow Field," *Proc. IMECE* (Orlando), HTD-vol. 366-1, pp. 229-235, November 2000.

[11] W. R. Lempert, K. Magee, P. Ronney, K. R. Gee, and R. P. Haugland, "Flow Tagging Velocimetry in Incompressible Flow Using Photo-Activated Nonintrusive Tracking of Molecular Motion (PHANTOMN)," *Experiments in Fluids*, vol. 18, pp. 249-257, 1995.

[12] R. F. Chen, G. G. Burek, and N. Alexander, "Fluorescence Decay Times: Proteins, Coenzymes, and Other Compounds in Water," *Nature*, vol. 156, pp 949-951, 1967.

[13] J. G Santiago, S. T. Wereley, C. D. Meinhart, D. J. Beebe, and R. J. Adrian, "A Particle Image Velocimetry System Microfluidics,", *Experiments in Fluids*, Vol. 25, No. 4, pp. 316-319, 1988.

[14] C. D. Meinhart, S. T. Wereley, and J. G. Santiago, "PIV Measurement of Microchannel Flow," *Experiments in Fluids*, Vol. 27, No. 5, pp. 414-419, 1999.

[15] F. M. White, *Fluid Mechanics*, fourth edition, Mcgraw-Hill, New York, 1999.

[16] W. M. Kays and M. E. Crawford, Third Edition, Mcgraw-Hill International Editions, 1993.

[17] B. R. Muson, D. F. Young and T. H. Okiishi, *Fundamentals of Fluid Mechanics*, John Wiley & Sons, New York, 1998.

[18] P. W. Runstadler, *Diffuser Data Book*, Technical Note 186, Creare, Inc., Hanover, NH, 1975.

[19] J. Bardina et al, "A Prediction Method for Planar Diffuser Flows," *Journal of Fluid Engineering*, Vol. 103, pp. 315-321, 1981.
[20] J. Coppeta, C. Rogers, "Dual emission laser induced fluorescence for direct planar scalar behavior measurements," *Experiments in Fluids*, vol. 25 pp. 1-15, 1998.
[21] J. Sakakibara, R. J. Adrian, "Measurement of whole field temperature using two-color LIF," *Journal of Visualization Society of Japan*, vol. 17, 333-336, 1997.
[22] D. L. Andrews, *Lasers in chemistry*, Springer-Verlag, Berlin, 1986.
[23] H. J. Kim, K. D. Kihm, and J. S. Allen, "Examination of a Ratiometric Laser Induced Fluorescence Thermometry for Microscale Spatial Measurement Resolution," *International Journal of Heat and Mass Transfer*, vol. 46, issue 21, pp. 3967-3974, 2003.
[24] J. R. Salor, "Photobleaching of Disodium Fluorescein in Water," *Experiments in Fluids*, vol. 18, pp. 445-447, 1995.

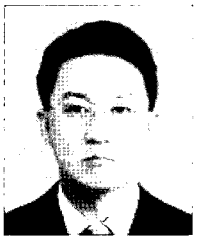

Han-Seo Ko
received his M.S. and Ph.D. degrees in Mechanical Engineering from Texas A&M University in 1994 and 1998, respectively. He has been an Assistant Professor in the School of Mechanical Engineering, Sungkyunkwan University, Korea since 2001. He is interested in Flow Visualization, Optical Tomography, Laser Technology, Image Processing, Fluid Dynamics, and Heat Transfer.

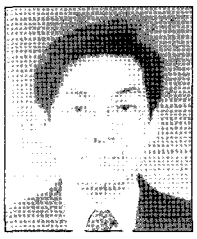

Sang-Sik Yang
received his Ph. D. degree in Mechanical Engineering from the University of California, Berkeley in 1988. He was then a Research Assistant Professor at the New Jersey Institute of Technology. Since 1988, he has been a Professor in the Division of Electronics Engineering at Ajou University. His research interests include the mechanism and actuation for microelectromechanical devices, motion control and non-linear control

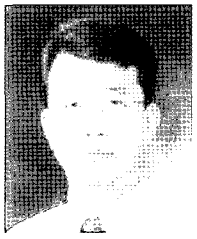

Jai-Suk Yoo
received his B.S and M.S. degrees in Mechanical Engineering in 1980 from Seoul National University. He received his Ph.D. in Mechanical Engineering in 1984 from the University of California, Berkeley. He has worked in the Division of Mechanical Engineering, Ajou University as a Professor since 1985. His research interests are nano fluidics, micro scale heat transfer and optical property measurement.

Hyun-Jung Kim
received his B.S and M.S. degrees in Mechanical Engineering in 1996 from Hanyang University. He received his Ph.D. in Mechanical Engineering in 2001 from Texas A&M University. He has worked in the Division of Mechanical Engineering, Ajou University as an Assistant Professor since 2003. His research interests are nano fluidics, micro scale heat and mass transfer and measurement with Micro PIV and LIF.